Novel ZnS-ZnO composite synthesized by the solvothermal method through the partial sulfidation of ZnO for H_2 production without sacrificial agent

Yanet Piña-Pérez[a,*], Octavio Aguilar-Martínez[a,*], Próspero Acevedo-Peña[b],
C.E. Santolalla-Vargas[c], Socorro Oros-Ruíz[a], Félix Galindo-Hernández[d], R. Gómez[a],
F. Tzompantzi[a]

[a] Depto. de Química, Área de Catálisis, Universidad Autónoma Metropolitana-Iztapalapa, Av. San Rafael Atlixco No. 186, Iztapalapa, Cd. de México 09340, Mexico
[b] CONACyT-Centro de Investigación en Ciencia Aplicada y Tecnología Avanzada, unidad Legaria, IPN, Cd. de México 11500, Mexico
[c] Departamento de Biociencias e Ingeniería, Centro Interdisciplinario de Investigaciones y Estudios sobre Medio Ambiente y Desarrollo (CIIEMAD), Instituto Politécnico Nacional, C.P. 07340 Cd. de México, Mexico
[d] Universidad Nacional Autónoma de México (CCH-O), Av. Canal de San Juan S/N, Tepalcates, 0920 Iztapalapa, Cd. de México, Mexico

ARTICLE INFO

ABSTRACT

Novel ZnS-ZnO composites were synthesized by the solvothermal method from the partial sulfidation of ZnO using thiourea at low temperatures. The synthesized materials were active for the photocatalytic production of H_2 with and without the presence of sacrificial agent without the addition of a co-catalyst; in the present paper, methanol was evaluated as sacrificial agent, increasing the amount of H_2 produced up to five times compared to the most active photocatalyst without using sacrificial agent. All the materials were characterized by XRD, N_2 Physisorption, FT-IR, XPS, Diffuse Reflectance Spectroscopy, and HR-TEM. In addition, the materials were characterized by photo-electrochemical techniques to explain the photocatalytic behavior. The most active material was the composite with an atomic ratio of S/Zn = 0.71 synthesized at 100 °C, producing 247 $\mu mol\ H_2\ h^{-1}\ g^{-1}$, the H_2 production rate was improved five times with the addition of methanol as sacrificial agent. The improvement of the photocatalytic activity was attributed to the formation of the heterojunction at the interface formed between ZnO and ZnS, promoting a higher electron transfer to the conduction band and a lower charge transfer resistance from the catalyst surface to the solution reaction.

1. Introduction

At present, there is a greater energy demand and a strong environmental problem due to the increase of population and industrial development, so it is of interest to promote new technologies to generate clean energy. Sunlight and water are renewable natural resources on earth and can be harnessed for the generation of clean fuels such as H_2 [1]. Unique properties of hydrogen make it a versatile, green chemical energy carrier suitable for all types of heat engines and other equipments. Taking into account this fact, the development of novel and efficient technologies to produce hydrogen, based on systems mimicking natural photosynthesis is of great interest to solve problems of energy shortage.

The use of semiconductor materials in photocatalysis is an alternative to obtain H_2 without damaging the environment. The water splitting through photocatalysis includes three steps; the first, is the light absorption by the semiconductor to form the electron-hole pairs,

in the second step, the migration of the charge carriers on the active sites located on the semiconductor surface, or, the recombination of the photogenerated electron-hole pairs occurs in the bulk material and finally, a redox reaction is carried out on the material surface, where the holes oxidize the H_2O molecule to transform it into O_2 and protons, while the electrons reduce the H^+ to form H_2 [2,3]. The positions of the valence and the conduction band play an important role in the water splitting process, the valence band must be more positive than the oxygen evolution reaction "OER" potential (+ 0.82 V relative to a SHE (standard hydrogen electrode) at pH 7.0), and the conduction band must be more negative than the hydrogen evolution reaction "HER" potential (− 0.41 V relative to a SHE at pH 7.0) [4]. The production of molecular hydrogen (H_2) by photocatalytic water splitting is energetically disadvantaged due to the rapid recombination of the electron-hole pairs and the slow kinetic for OER; however, the use of sacrificial agents increases the production rate of H_2 [5]. The field of photocatalytic H_2 production using carbon-compounds as sacrificial

agents has gained significant attention. Among them, methanol has been widely used as a sacrificial agent for H_2 production by photocatalysis, owing to its simple structure that helps to understand the reaction mechanism, and this molecule acts like a hole-scavenger. Also, this alcohol can be easily mineralized producing less toxic substances [6]. It has been reported that alcohols have a strong tendency to react with holes and thus suppress the recombination and therefore an increase on the H_2 production is observed. An important point to note here is that, in the presence of alcohols, the lifetimes of photo-generated holes are significantly shorter (10^{-12}–10^{-9} s) than those of photo-generated electrons (10^{-5}–10^{-3} s) [7], since the alcohols act as a hole trap avoiding the recombination process.

A key problem in photocatalytic water splitting over disperse semiconductor photocatalysts is the recombination of the electron-hole pairs in the bulk or on the surface of semiconductors. Nevertheless, improved spatial separation of photogenerated charges allows to increase the quantum efficiency of hydrogen production [8]. The combination of different semiconductors to create composites is an alternative to overcome the recombination and create new materials with enhanced photocatalytic properties for H_2 production since the separation of the charge carriers is favored due to the formation of heterojunctions [3,9]. Recently, several types of photocatalytic composite materials have been used to improve the photocatalytic activity, for example, Bi_2O_3-TiO_2 [10], MoS_2/RGO layers as cocatalyst on CdS [11], WS_2-CdS [12], among others [13]. In the present work, the use of ZnS coupled with ZnO throughout a heterojunction is proposed. The position of the valence and conduction band of ZnS make possible to carry out the photocatalytic process for the H_2 production [14]; the addition of ZnO may contribute to the separation of the electron-hole pairs to increase the H_2 production. It has been reported that ZnS-ZnO is an efficient composite for the photocatalytic production of H_2 using sacrificial agents [15–24]; however, in this work it is shown that ZnS-ZnO composite is also capable to generate H_2 without using any sacrificial agent. This composite can be obtained by several synthesis routes, for example, it can be obtained from its precursors (Zn^{2+} and S^{2-}) [25], from the partial sulfidation of ZnO [26], and partial oxidation of ZnS [17], the last two methods have the inconvenient that have to be carried at high temperatures ($> 200\,°C$); however in this work the solvothermal method has been employed to obtain the ZnS-ZnO material by the partial sulfidation of ZnO at low temperatures ($\leq 100\,°C$). These composites proved to be efficient for the H_2 production without using any sacrificial agent, which has not been previously reported for this type of materials.

ZnS-ZnO composites were synthesized through the partial sulfidation of ZnO at 80, 100, and 150 °C. The material with the higher photocatalytic activity was the composite synthesized at 100 °C with an atomic ratio of S/Zn = 0.71. The high activity was attributed to the formation of a heterojunction, which improves a high charge transfer, in other words, a greater accumulation of electrons and holes is generated at the conduction and the valence band, respectively. Additionally, using methanol as sacrificial agent, the photocatalytic activity increased up to five times the H_2 production for the most active photocatalyst, since holes are rapidly transferred to methanol molecules in the interface avoiding the recombination, enhancing the quantum yield [27]. The ZnS-ZnO composites were efficient for the H_2 production with and without sacrificial agent in the presence of UV light ($\lambda = 254$ nm).

2. Experimental procedure

2.1. Materials synthesis

2.1.1. ZnO synthesis

The **ZnO** was obtained from the calcination of $Zn_5(CO_3)_2(OH)_6$ at 300 °C (see the Fig. 1S at the supplementary information); this was obtained by the precipitation method. Zinc nitrate hexahydrate (Zn$(NO_3)_2$·$6H_2O$, Meyer, 99%) and urea (NH_2CONH_3, Reasol, 99%), in a molar ratio 1:3, were dissolved in 600 mL of distilled water. This mixture was kept under vigorous stirring at 90 °C for 72 h. The precipitated powder was filtered and washed using distilled water, and subsequently, dried at 100 °C for 24 h. The synthesized $Zn_5(CO_3)_2(OH)_6$ was pulverized and annealed at 300 °C using heating rate of 0.5 °C min^{-1} for 3 h, to obtain the **ZnO**. The annealing temperature was selected from the thermogravimetric analysis (Fig. 2S).

2.1.2. ZnS-ZnO composites synthesis

These materials were prepared by the solvothermal method using ethanol as solvent and thiourea as S^{2-} source. Initially, 0.012 mol of the synthesized **ZnO** and an excess of thiourea (CH_4N_2S, Reasol, 99.0%) were put in a glass flask; then 100 mL of ethanol (C_2H_5OH, Meyer, 96°) were added, and the mixture was sonicated for one hour. Then, the pH was adjusted using ethylenediamine ($C_2H_8N_2$, Sigma-Aldrich, 75–80%) to an alkaline pH of 12.0, and subsequently, the mixture was put into a Parr reactor for 5 h under magnetic stirring. The composite materials were obtained by using different temperatures 80, 100, and 150 °C in the Parr reactor. The synthesized powders were filtered and washed with 250 mL of ethanol and 500 mL of distilled water, and finally were dried at 80 °C for 12 h. The sulfided materials were labeled as **ZS80**, **ZS100**, and **ZS150**, respectively.

The elemental composition of each photocatalyst was obtained by using X-ray Photoelectron Spectroscopy (XPS) (Fig. 4S). The atomic ratios of S/Zn for the **ZS80**, **ZS100**, and **ZS150** materials were 0.55, 0.71 and 0.80, respectively; the chemical composition of each material is summarized in Table 1.

2.2. Characterization techniques

X-ray diffraction patterns were obtained on a D2 Phaser Bruker diffractometer with the Bragg-Brentano θ–θ geometry, CuKα radiation equipped with a Lynxeye detector. Intensities were obtained in the 2-theta ranges between 20 and 85° with a step of 0.01° and a measuring time of 6 s per point. The crystalline structures were refined by the Rietveld method using the TOPAS-Academic software [28]. For the refinement of ZnO structures (Table 1S), a hexagonal lattice of 47.601 Å^3 with two atoms, Zn:O ratio of 2:2 and space group *P63mc* (186) data were used, and for ZnS structures (Table 2S), eighty atoms, Zn:S ratio of 2:2 and hexagonal lattice of 315.431 Å^3 and space group *P63mc* (186) data were employed. The theoretical crystal density (see Tables 1S and 2S) was calculated by the following equation [29]:

$$\rho_{crystal} = \frac{(Z)(MM)(Avogadro's\ number)^{-1}}{Cell\ volume} \tag{1}$$

where Z is the number of molecules cell^{-1} and MM is the molecular weight.

The atomic fractional coordinates shown in Tables 1S and 2S, were chosen from the crystallographic tables according the theoretical density. Infrared spectroscopy was obtained on a FT-IR Affinity-1Shimadzu spectrophotometer from 4000 to 400 cm^{-1}, using 200 scans and a resolution of 8.0 cm^{-1}. Diffuse reflectance spectroscopy was measured as a function of wavelength from 190 to 600 nm on a Varian Cary-100 spectrophotometer equipped with an integrating sphere accessory and using $BaSO_4$ as reference. N_2 adsorption-desorption isotherms of the materials were determined on an Autosorb-3B (Quantachrome) equipment. Prior to these measurements the powders were desorbed at 100 °C for 12 h. The specific surface areas were obtained using the BET method. X-ray photoelectron spectroscopy (XPS) was carried out using a K-alpha Thermo Fischer Scientific spectrometer with a monochromatic Al Kα radiation (1486.6 eV) as an X-Ray source and were microfocused at the source to give a spot size on the sample of 400 microns of diameter. In order to compensate effects related to charge shifts, C1s peak at 284.6 eV was used as internal standard. High-resolution transmission electron microscopy (HR-TEM) images of the
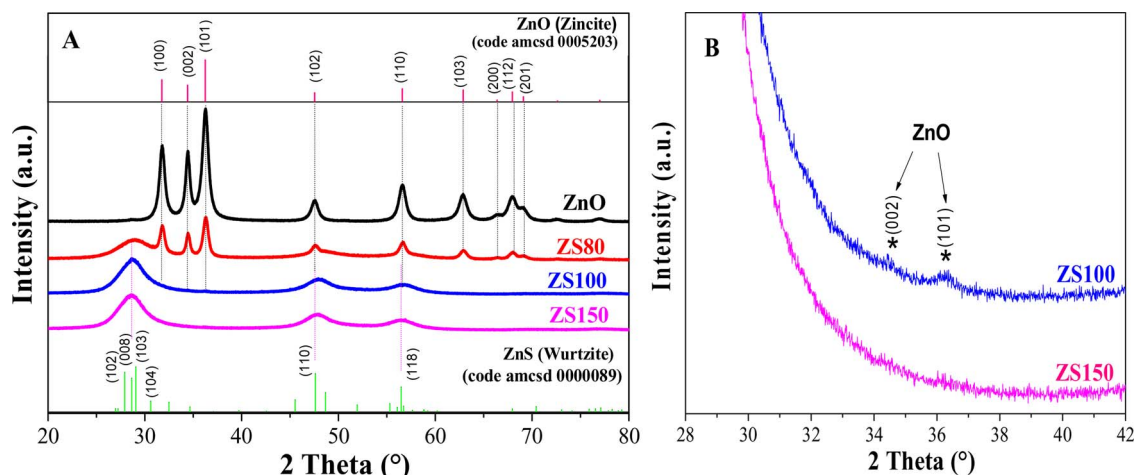
Fig. 1. A. X-ray diffraction patterns of the **ZnO**, **ZS80**, **ZS100**, and **ZS150** materials. B. X-ray diffractogram amplification of the **ZS100** and **ZS150** photocatalysts.
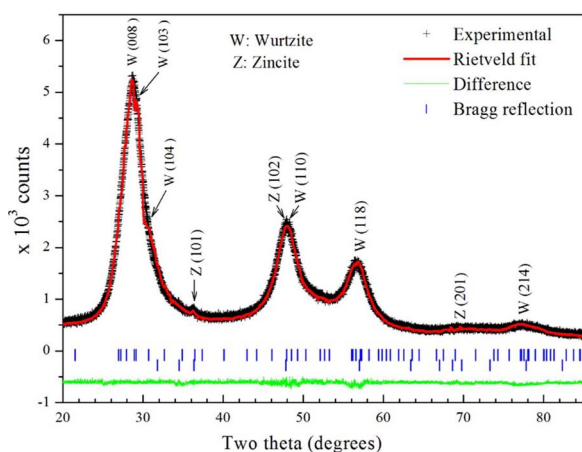

Fig. 2. Rietveld plot for **ZS100** material ($R_p = 3.8$, $R_{wp} = 5.0$, $R_{exp} = 2.8$). It has two phases: wurtzite (upper tick marks) and zincite (lower tick marks). The upper curve crosses correspond to the experimental data and the continuous line corresponds to those calculated; the lower curve is the difference of both data. The numbers in parenthesis corresponds to different diffraction planes (hkl) of the crystalline structures.

Table 1
Band gap energy (Eg), specific surface area (SSA), and composition of atomic elementary percent of the **ZnO**, **ZS80**, **ZS100**, and **ZS150** materials.

Material	Eg (eV)	SSA ($m^2 g^{-1}$)	Atomic %[a]					S/Zn Ratio
			Zn	S	O	C	N	
ZnO	3.1	64	43.0	–	42.8	14.2	–	–
ZS80	3.2	139	34.4	18.8	18.9	21.7	6.2	0.55
ZS100	3.6	210	37.7	26.8	8.3	17.6	9.6	0.71
ZS150	3.6	103	28.6	22.8	6.3	26.8	15.5	0.80

[a] Data obtained from XPS.

samples were collected on a JEM-ARM 200CF microscope operated at 200 kV. The high-resolution images were digitally captured by a Gatan CCD digital camera. The interplanar distances and the inverse Fast Fourier Transform (FFT) were calculated using the Digital Micrograph software.

2.3. Photocatalytic test

The photocatalytic evaluation for the materials was carried out in a homemade batch glass reactor with cylindrical shape (5.5 cm of diameter and 270 mL of capacity). The light source used was a mercury lamp (UV Pen-Ray) with a wavelength of 254 nm, equivalent to 4.8 eV, and a radiation power of $6.0 \, mWcm^{-2}$ measured on a UVX digital radiometer. The lamp was protected by a quartz tube and it was placed inside of the photocatalytic reactor. For each reaction, 100 mg of catalyst were added to 200 mL of water or 200 mL of a methanol-water solution (1:1, vol.), depending on the case. Throughout the photocatalytic reaction, the system was kept under magnetic stirring at room temperature. The amount of H_2 produced was determined by sampling every hour on a gas chromatograph equipped with a Shin-carbon column and a TCD detector by using a calibration curve and N_2 as carrier gas.

2.4. Photo-electrochemical tests

A conventional three-electrode cell was employed to perform the photo-electrochemical characterization of the photocatalysts. An electrode Ag/AgCl/0.1 M KCl was used as reference electrode. The counter electrode was a graphite rod. To prepare the photocatalysts films (working electrodes), 100 µL of 30 mg mL^{-1} ZSx suspension in ethanol, were deposited on a clean ITO coated substrate (Aldrich, Rs = 15–25 Ω cm^2) of 1.25 × 2.5 cm, which were placed inside of a spin coater at 1000 rpm for 30 s. The as prepared photocatalysts films were dried at 80 °C for 2 h to evaporate as much solvent as possible. Finally, a squared area of 0.5 × 0.5 cm was delimited to perform the measurements [30]. The electrochemical characterization was performed using a 0.03 M NaClO$_4$ in water or 1:1 water:methanol electrolyte. Previous to each measurement, N$_2$ was bubbled for 15 min. The illumination was performed using a Newport Q Housing (Model 60025) equipped with a 100 W Hg arc lamp. The semiconducting properties were estimated from MottSchottky plots, the space charge capacitance of the films was measured in dark conditions at a frequency of 400 Hz. EIS measurements were performed at the open circuit potential using an AC perturbation of ± 25 mV. All measurements were carried out using an AUTOLAB 302N potentiostat.

3. Results and discussion

3.1. X-ray diffraction

Fig. 1A shows the crystallographic planes of **ZnO**, **ZS80**, **ZS100**, and **ZS150** materials. **ZnO** shows the diffraction planes corresponding to the hexagonal zincite phase (data base code amcsd 0005203). The peaks were detected at 2θ° at 31.8, 34.4, 36.3, 47.5, 56.6, 62.9, 66.4, and 68.0°, corresponding to the plans (100), (002), (101), (102), (110), (103), (200), and (112), respectively. Additionally, peaks were found at 28.5, 47.6, and 56.4° for the sulfided materials, corresponding to the
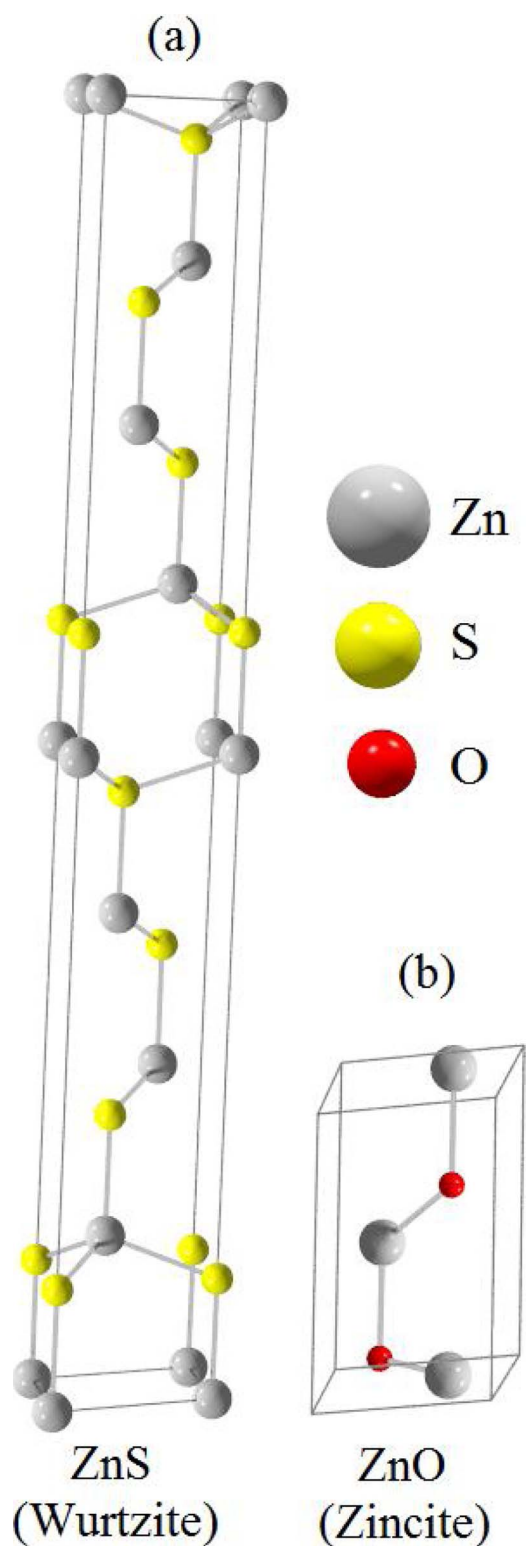
(a)

Zn

S

O

(b)

ZnS
(Wurtzite)

ZnO
(Zincite)

Fig. 3. (a) Lattice of ZnS crystal: Hexagonal with a = b = 3.8200 Å and c = 24.9600 Å. (b) Lattice of ZnO crystal: Hexagonal with a = b = 3.2490 Å and c = 5.2070 Å.

crystallographic planes (008), (110), and (118), respectively, of the ZnS wurtzite type 8H (data base code amcsd 0000089). While increasing the synthesis temperature, the intensity of the characteristic peaks of ZnO decreases and an enhancement on the ZnS diffraction peaks is observed, indicating the formation of the ZnS-ZnO composite materials. It should be noted from the X-ray diffraction patterns of the **ZS150** sample, only peaks corresponding to hexagonal ZnS were observed. The widening of

the observed peaks of the **ZS100** and **ZS150** materials is due to the contribution of the different diffraction planes of ZnS, as observed in the standard data of ZnS wurtzite inserted at the bottom of the Fig. 1. For the **ZS80** composite, the characteristic peaks of both components ZnS and ZnO are present. However, for the composite labeled as **ZS100**, small traces of ZnO are observed (see Fig. 1B). Fig. 2 shows the Rietveld plot for **ZS100** material, performed by the lattice parameters of zincite and wurtzite respectively (see Tables 1S and 2S). Diffraction planes (hkl) corresponding to zincite and wurtzite structures are observed. For **ZS100** material, a composition of 99.72 and 0.28 wt.% of wurtzite and zincite phases with densities of 4.192 and 5.675 g cm^{-3} were found (see Table 3S). Fig. 3a and b show the ZnS and ZnO lattices displaying the contact areas between them. Although, there are not significant changes on the crystal densities after comparing the theoretical values vs those obtained by Rietveld refinement, the zincite structure is 35.37% denser than the wurtzite structure which might improve the mechanical properties of the **ZS100** material.

3.2. Infrared spectroscopy

The FT-IR measurements of the materials were carried out and the representative bands were identified (see Fig. 3S). For the zinc oxide, the band located between 1100–620 cm^{-1} corresponding to the vibration of CO_3^{2-} groups was observed, and it was attributed to residues of the $Zn_5(OH)_6(CO_3)_2$ precursor; the most intense peak around 550 cm^{-1} corresponds to the vibration of Zn−O [31–33]. On the other hand, the sulfided materials showed a wide band, between 3700 and 3000 cm^{-1}, characteristic of the −OH vibration, in addition, another band observed at 1600 cm^{-1}, correspond to the different vibrational modes of the −OH group of the physisorbed water. The bands centered at 2947, 2879, 1550, and 1020 cm^{-1} correspond to the vibrational modes of the −CH, −CH$_2$, −NH$_2$ and C−N groups, respectively. The presence of these bands indicate that the ethylenediamine molecules are linked to the surface of the sulfided materials [34]. Finally, the band located at 665 cm^{-1} was assigned to Zn−S vibration [35].

It is observed, that the band centered at 1550 cm^{-1}, corresponding to the −NH$_2$ vibration, increases its intensity as the temperature of the synthesis increases, indicating the increment of ethylenediamine on the surface. These results are consistent with the elemental analysis quantified by low resolution of XPS measurements (see Fig. 4S), the atomic percentage of each detected element is summarized in Table 1. The increase of the S, N, and C contents was observed as the synthesis temperature increases, in agreement with the FT-IR measurements; atomic ratios of S/Zn of 0.55, 0.71, and 0.80 were found for the **ZS80**, **ZS100**, and **ZS150** materials, respectively.

3.3. Diffuse reflectance spectroscopy

Fig. 4A shows the diffuse reflectance spectra, F(R), as a function of the wavelength for the synthesized materials. **ZnO** presents the absorption edge around 400 nm, which is characteristic of this oxide; while the **ZS150** material shows its absorption edge at 345 nm characteristic of materials mainly composed of ZnS, as it was also observed by X-ray diffraction (see Fig. 1A), this material presents a tail on the absorption from 345 to 600 nm, attributed to the superficial defects caused by ethylenediamine molecules that are linked to the ZnS surface [15], as seen in the FT-IR characterization. The composites **ZS80** and **ZS100** have their absorption edges between 345 and 400 nm. The displacement of the absorption edge towards lower wavelengths is attributed to the increase of ZnS content. The band gap energy values were calculated by using the Tauc's plot (Fig. 4B). Allowed direct transitions were considered for **ZnO** and the sulfided materials [36–38]. The band gap energy values for the **ZnO**, **ZS80**, **ZS100**, and **ZS150** materials were 3.1, 3.2, 3.6 and 3.6 eV, respectively (see Table 1).
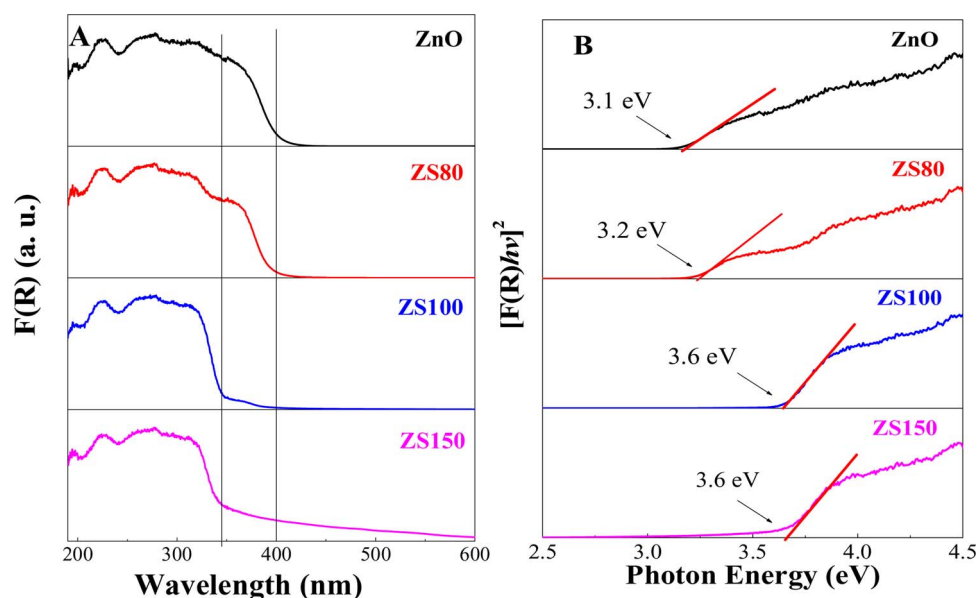
Fig. 4. A. Diffuse reflectance spectroscopy, F(R) versus wavelength, and B. Tauc's plot of the **ZnO**, **ZS80**, **ZS100**, and **ZS150** materials.

3.4. Textural properties

The Fig. 5 shows the measurements of the N_2 adsorption-desorption isotherms of the bare **ZnO** and **ZS80**, **ZS100**, and **ZS150** sulfided materials. It was found that the isotherms correspond to type IV, according to the IUPAC classification [39], for all the photocatalysts. This type of isotherm is characteristic of mesoporous materials. For the **ZnO** and **ZS80** composites, the hysteresis loop correspond to type H3 [39], this type is attributed to non-rigid aggregates of plate-like particles, with no uniform size; however, the **ZS100** and **ZS150** photocatalysts present hysteresis loop type H4 associated to slit-shapes, pore as plate, with uniform size and shape [40]. The change in the hysteresis loop from H3 to H4 is due to the increase in the content ZnS. The BET specific surface areas for the **ZnO**, **ZS80**, **ZS100**, and **ZS150** materials were 64, 139, 210, and $103\,m^2\,g^{-1}$, respectively. The presence of both phases, ZnO and ZnS, in the **ZS80** and **ZS100** composite materials favors the improvement in the specific surface area, especially for the **ZS100** material containing an atomic ratio S/Zn of 0.71, as has been reported in other studies [15,41,42]. For materials having this composition, it has been observed a change on the morphology of different mesoporous structures generating a greater specific surface area with respect to the bare ZnO and ZnS materials [15].
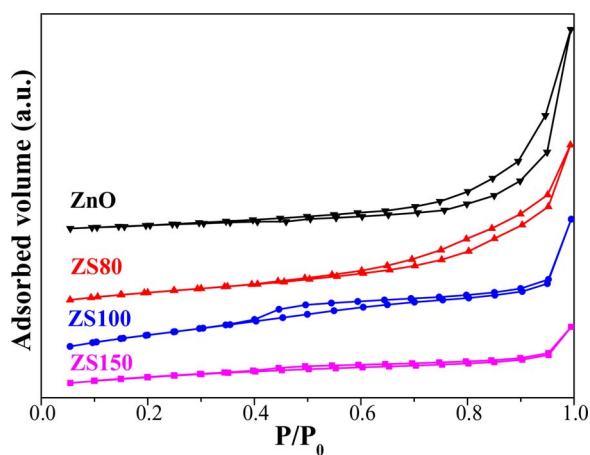
3.5. High resolution transmission electron microscopy

HR-TEM was performed for the selected **ZS80** composite with the purpose of determining the existence of a heterojunction formed between ZnO and ZnS in the partially sulfided materials. The HR-TEM of the **ZS80** material (Fig. 6) shows the interplanar distance of 0.259 nm corresponding to the (002) plane of hexagonal ZnO, on the other hand, the interplanar distance of 0.307 nm corresponds to the (103) plane of ZnS wurtzite [43]. The inset chart shows the heterojunction formed between wurtzite (ZnS) and zincite (ZnO), at the **ZS80** composite. The existence of a heterojunction between the two components reflects that they are chemically bounded as a consequence of the synthesis method used to obtain these photocatalysts.

3.6. Photocatalytic test

The photocatalytic test for H_2 production was carried out for the synthesized materials with and without the presence of a sacrificial agent. Fig. 7A shows the quantity of H_2 produced (µmol) as a function of the reaction time in the absence of a sacrificial agent. Hydrogen is not produced in the absence of photocatalyst (photolysis reaction) a similar behavior was observed for **ZnO** and **ZS150** samples evidencing that these materials do not perform the thermodynamic and kinetic requirements for water splitting. In contrast, **ZS80** and **ZS100** samples showed a higher H_2 production by water splitting. The Fig. 7B shows
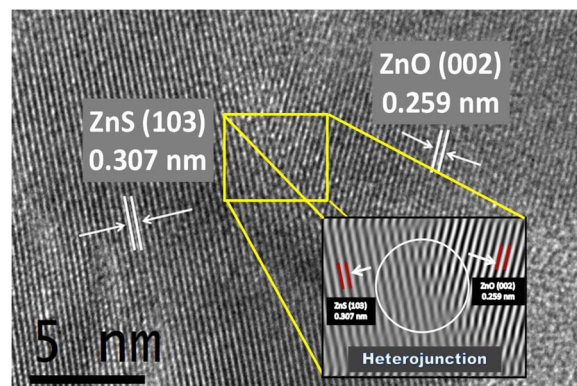

Fig. 5. N_2 Adsorption-desorption isotherms of the **ZnO**, **ZS80**, **ZS100**, and **ZS150** materials.

Fig. 6. HR-TEM of the selected **ZS80** composite. The inset shows the inverse FFT.
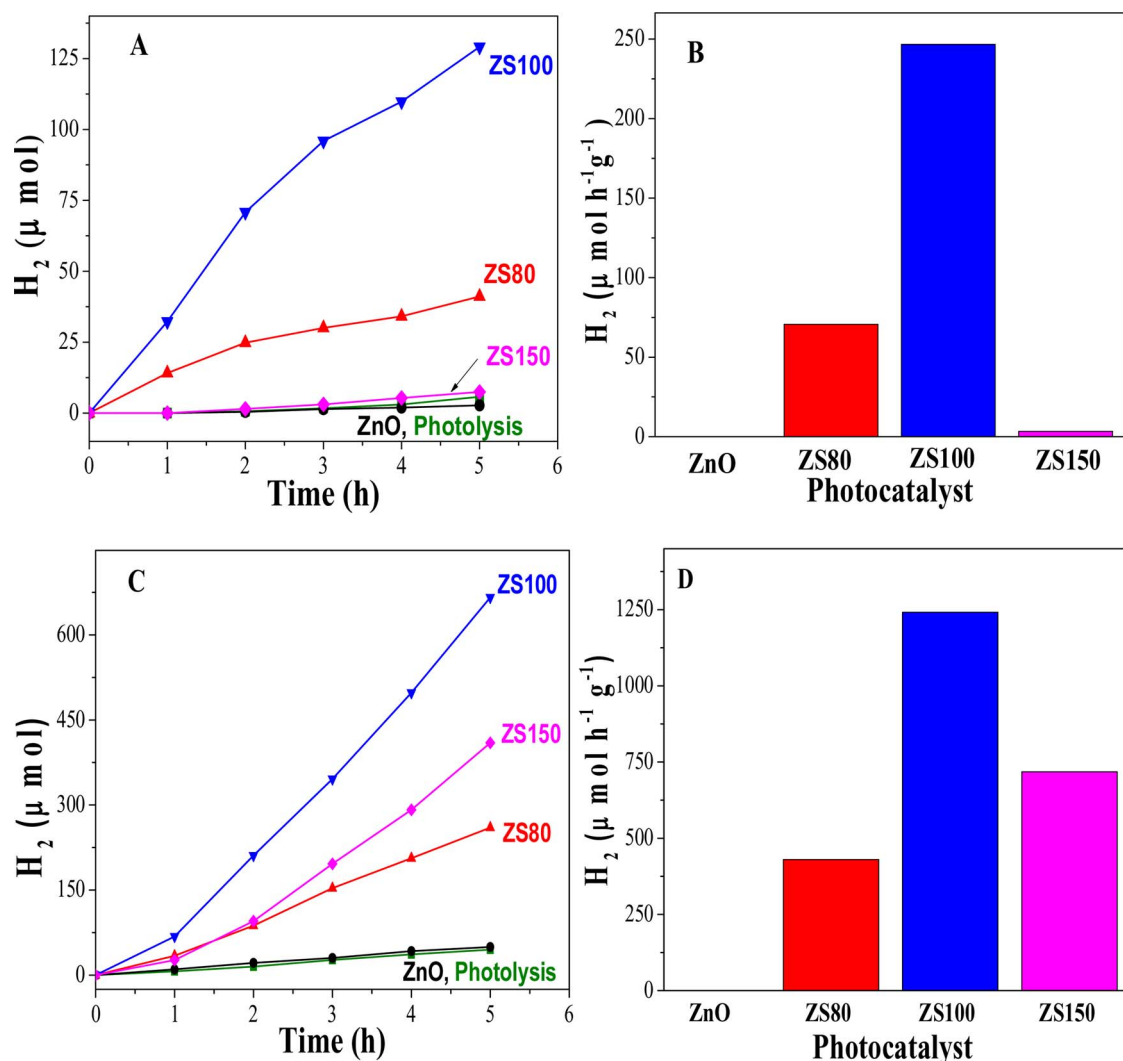
Fig. 7. Evolution of H_2 by **A.** water splitting and **C.** water-methanol. H_2 production rate by **B.** water splitting and **D.** water-methanol of the synthesized materials.

Table 2
Flat band potential (E_{fb}), charge transfer resistance (R_{ct}), H_2 production rate and apparent quantum yield (AQY) of the **ZnO**, **ZS80**, **ZS100**, and **ZS150** materials (with and without sacrificial agent).

Material	Absence of sacrificial agent				Using sacrificial agent			
	E_{fb} (V)	R_{ct} (kΩ cm^2)	H_2 (μ mol h^{-1} g^{-1})	AQY (%)	E_{fb} (V)	R_{ct} (kΩ cm^2)	H_2 (μ mol h^{-1} g^{-1})	AQY (%)
ZnO	−0.50	28.1	–	–	−0.56	3.7	–	–
ZS80	−0.53	278.8	71	1.6	−0.79	249.1	430	9.6
ZS100	−1.14	177.2	247	5.5	−1.29	104.8	1242	27.6
ZS150	−0.96	1759.4	–	–	−0.96	135.8	718	15.9

the rate of H_2 production per gram of catalyst. The **ZS100** composite showed the highest photo-activity with a production rate of 247 μ mol h^{-1} g^{-1} followed by the **ZS80** composite with 71 μ mol h^{-1} g^{-1} (see Table 2). These results suggest that there is an optimum content of ZnO and ZnS at the composite that favors an improvement of the photocatalytic activity. This result is of particular interest, since the hydrogen production in absence of sacrificial agent (water splitting), using ZnS-ZnO composite, has not been previously reported.

We have to keep in mind that the photocatalytic processes always include at least two half-reactions, and the overall rate of the process is determined by the slowest step, in this case the oxygen evolution reaction. The use of sacrificial agents as hole scavengers delay the

electron-hole recombination leaving more electrons available to perform the reduction reaction, so, there is an improvement on the rate of H_2 production. It is well known that methanol is a good hole scavenger, so, in this work it was used as sacrificial agent for comparison. The Fig. 7C shows the H_2 production of the synthesized materials as a function of the reaction time, as well as, the photolysis reaction, using a methanol-water solution (1:1 vol). For all the sulfided materials, there was an enhancement on the H_2 production with the irradiation time; however, **ZnO** did not show an improvement for the H_2 evolution compared to the photolysis reaction. The rate of hydrogen production per gram of catalyst improved as the ZnS content increases (Fig. 7D), reaching a maximum when the material is composed for an atomic ratio of S/Zn = 0.71 (**ZS100**). At higher synthesis temperatures above

100 °C, the photocatalytic activity decreases as it was show by the **ZS150** material. It is worth pointing out, that the use of methanol as sacrificial agent increased up to five times the H_2 production for the most active material, acting as a hole scavenger, and decreasing the process of electron-hole recombination. It is worth to mention that, in Fig. 7C, an induction period is observed during the first hour of H_2 production for all the sulfided materials; after this reaction time, the H_2 production follows a linear behavior. The induction period may be associated to the presence of methanol molecules, since in water splitting without sacrificial agent it is not observed. Possibly, at the first minutes of reaction, the adsorption or interaction of methanol on the material surface is carried out inhibiting the H_2 evolution, also, it has been reported, that this induction period is associated to the formation of intermediaries during the oxidation of the methanol molecule [44].

Quantum yield is another important indicator for the photocatalytic activity of the semiconductor materials. However, it is difficult to determine the real number of photons absorbed by a photocatalyst in a dispersed system. To address this problem, it has been assumed that all the incident photons are absorbed by the photocatalyst and the corresponding quantum yield is called the apparent quantum yield (AQY). As shown in the eq. 2, the apparent quantum yield can be measured from the amount of H_2 produced in the photocatalytic reaction and the number of incident photons, the coefficient 2 means that two electrons are necessary for the formation of one hydrogen molecule, and, correspondingly, it is required that two photons interact with the catalyst [45,46].

$$AQY = \frac{2(Number\ of\ H_2\ molecules\ produced/s)}{N\ photon/s} x100\% \quad (2)$$

$$NS = N_{photon}\varphi_i\sum_i h\frac{c}{\lambda_i} \quad (3)$$

The number of incident photons can be obtained from the eq. 3. Where N is the radiation power of the lamp and was measured experimentally using a radiometer ($0.006\ W\ cm^{-2}$), S is the light spot area ($19.76\ cm^2$), λ_i is the ith wavelength peak, φ_i is the relative intensity of the ith peak, h is the Planck constant, c is the speed of light, and N_{photon} is the number of photons.

The Hg lamp used emits three wavelengths in the UV region; 185, 254, and 313 nm with relative emissions intensities of 3.0, 94.5, and 2.5%, respectively. The number of measured photons was $1.50 \times 10^{17}\ photon\ s^{-1}$. The AQY (%) was obtained by applying the eq. 2. The highest apparent quantum yield was 5.5 and 27.6% for the **ZS100** material with and without sacrificial agent, respectively, the AQY (%) obtained for the other semiconductors can be found in the Table 2.

In addition, the reaction rate was normalized with respect to the BET specific surface area of the synthesized materials. In water splitting, in the absence of sacrificial agent, the normalized reaction rates were 0.0, 0.5, 1.2, 0.0 $\mu mol\ h^{-1}\ g^{-1}\ m^{-2}$, for the **ZnO, ZS80, ZS100,** and **ZS150** materials, respectively, for the case of H_2 evolution in presence of methanol, the normalized values with respect to the BET area were 0.0, 3.1, 5.9, and 6.9 $\mu mol\ h^{-1}\ g^{-1}\ m^{-2}$, for the **ZnO, ZS80, ZS100,** and **ZS150** materials, respectively. These values were different between them in each material for the both cases, so, the rate of H_2 production is not related to the surface area, this suggests that there are other processes involved that promote the enhancement of the photocatalytic activity, for example, the high accumulation of electrons at the conduction band and holes in the valence band, additionally, to the lower charge transfer resistance of the photocatalyst, as it will be discussed later in the photo-electrochemical characterization.

Finally, the stability of the most active photocatalyst was evaluated using the conditions that provide a greater H_2 production, (using methanol as sacrificial agent). The Fig. 8 shows five consecutive reaction cycles of the **ZS100** material. Reaction cycles were performed with the same methanol-water solution and purging with N_2 between each cycle.
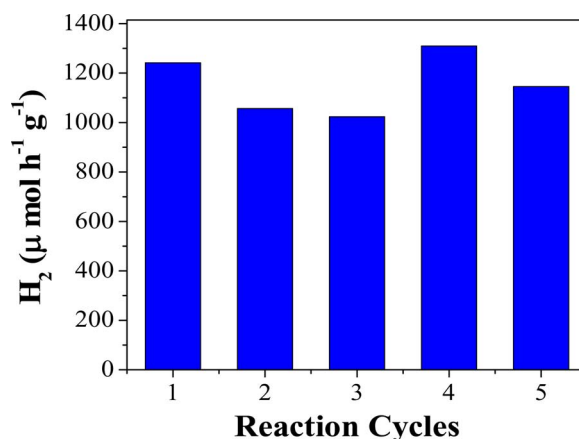

Fig. 8. First five reaction cycles of the **ZS100** composite using methanol as sacrificial agent.

The results show that the photocatalytic activity was maintained during the reaction cycles, indicating that the material is photochemically stable.

3.7. Photo-electrochemical characterization

In order to explain the behavior of the photocatalytic activity of the synthesized materials from the partial sulfidation of **ZnO**, some photo-electrochemical tests were carried out. Mott-Schottky characterization of the materials (Fig. 5S) shows that flat band (E_{fb}) potential of the composite displaces towards more negative values as the temperature of the synthesis increases reaching a maximum at 100 °C (**ZS100**), see Table 2. The displacement of the E_{fb} towards more negative values have been previously correlated to the formation of heterojunctions that provide a path for the separation of the charge carriers improving the photocatalytic activity of the materials [15,47]. The E_{fb} values obtained in presence of methanol are more negative than those measured in pure water, proving that methanol is strongly adsorbed on the surface of the photocatalyst. The presence of methanol represents another advantage over pure water since not only a new and more rapid oxidation reaction is present, but also the conduction band of the materials is shifted towards more negative values offering a larger potential difference to perform the H_2 evolution reaction. It is worth to point out, that the conduction band of all the synthesized materials is more negative that the thermodynamic potential required to reduce water at neutral pH ($\approx 0.42\ V$ vs SHE), however, the material with the larger difference between the E_{fb} and water reduction potential was **ZS100** and this material was the one that exhibited the best photocatalytic performance.

Photovoltage and EIS under illumination were measured using a 0.03 M $NaClO_4$ electrolyte in absence (Fig. 9A and B) and in presence (Fig. 9C and D) of methanol, previously bubbled with N_2. When the materials were illuminated, a negative photovoltage was generated, indicating that all of the materials behave as n-type semiconductors, which is in line with the Mott-Schottky measurements in Fig. 5S. The photovoltage generation has been correlated to the accumulation of electrons at the conduction band or the states below it. For both cases, (with and without methanol), the photovoltage generated increases with the percentage of sulfidation of **ZnO** (Fig. 9A and C), reaching a maximum for the material synthesized at 100 °C (**ZS100**), the same behavior was observed on its photocatalytic activity (see Section 3.6). The presence of methanol increased the generated photovoltage for the composite materials. This is attributed to the tuning of the conduction band position and the increase of the hole transfer reaction, leading to a larger number of electrons capable to perform the reduction reaction. The increase on the photovoltage in the presence of methanol was particularly remarkable for those composites with the highest content
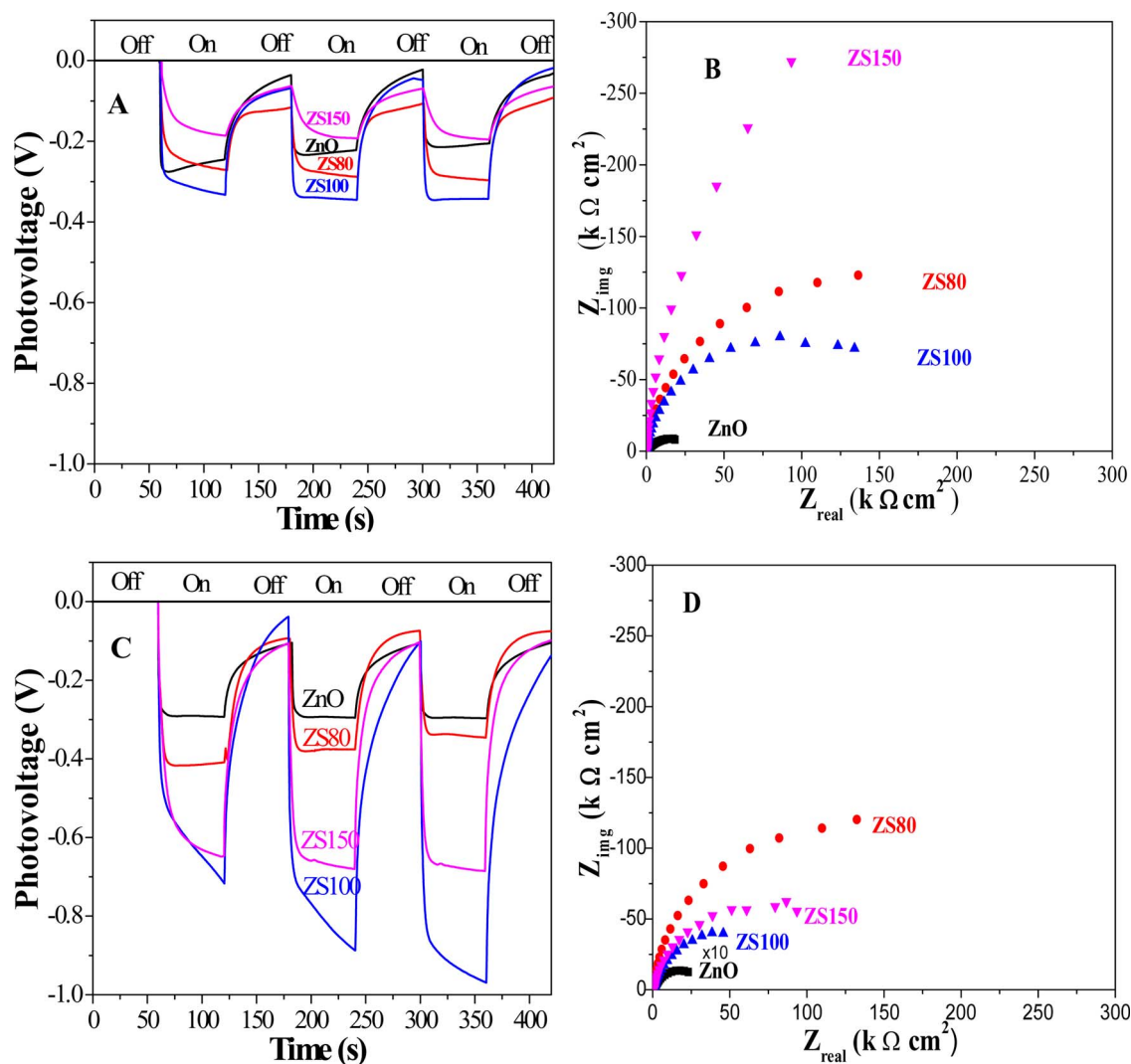
Fig. 9. Photo-electrochemical characterization of the synthesized photocatalysts supported on ITO in a 0.03 M NaClO$_4$ electrolyte. Variation of open circuit potential (OCP) versus time, three disturbances on and off were performed to evaluate the accumulation of photogenerated electrons in the photocatalyst, A. in water, C. in water-methanol. And EIS behavior at open circuit potential, measured under illumination B. in water, D. in water-methanol.

of ZnS, which explains why the **ZS150** composite passed from non-active to an active behavior in the photocatalytic tests without and with the presence of methanol, respectively (Fig. 7).

The impedance has been extensively used to measure the charge transfer resistance when the photocatalyst is illuminated. This technique is advantageous since the measurement was performed under similar conditions to those employed during the photocatalytic test (specifically, without imposing an external bias), and offers direct information over the kinetic of the processes occurring at the electrolyte/ photocatalysts interface under illumination.

The Nyquist diagrams for all the composites were measured in the absence and presence of methanol, and are shown in Fig. 9B and D, respectively. For all cases, R$_{ct}$ (diameter of the semicircle formed) takes lower values in the presence of methanol, see Table 2. Surprisingly, the material with the lower charge transfer resistance R$_{ct}$ is the **ZnO**; however, it is clear from the photocatalytic test in Fig. 7 that the H$_2$ evolution under illumination is not carried out due to its reduction potential position, and the changes on R$_{ct}$ are due to the high oxidant potential of holes in **ZnO**. For the case of the composite materials, **ZS100** always exhibited the lower impedances matching well with the highest H$_2$ generation rate, see Table 2, and the drastic change in the R$_{ct}$ between both cases for **ZS150** evidences that the photocatalytic hydrogen production was kinetically impeded in the absence of methanol

(Fig. 7).

3.8. Reaction mechanism

According to the previously discussed results, it was found that the material that generated the highest H$_2$ production with and without the presence of sacrificial agent was the composite with an atomic ratio of S/Zn = 0.71, synthetized at 100 °C. The textural characterization of the materials showed that **ZS100** composite presented the largest surface area, offering more active sites available to perform the HER. However, the generation of a heterojunction between ZnO and ZnS (see Fig. 6) was the origin of the remarkable performance of the **ZS100** composite [48]. In addition, the photo-electrochemical tests explained the results of H$_2$ production with and without sacrificial agent. First, the photocatalytic activity increases as the accumulation of electrons and holes increases on the conduction and valence band of the material, respectively. Second, the H$_2$ evolution is improved when the material shows a lower charge transfer resistance at the catalyst surface/solution reaction interface. It is worth to mention that, **ZnO** was the material that presented the lowest charge transfer resistance (Fig. 9B and D), however, the position of its conduction band with respect to the hydrogen reduction potential does not make possible the reduction of H$^+$ to H$_2$. Finally, when ZnS and ZnO semiconductors get in contact, new
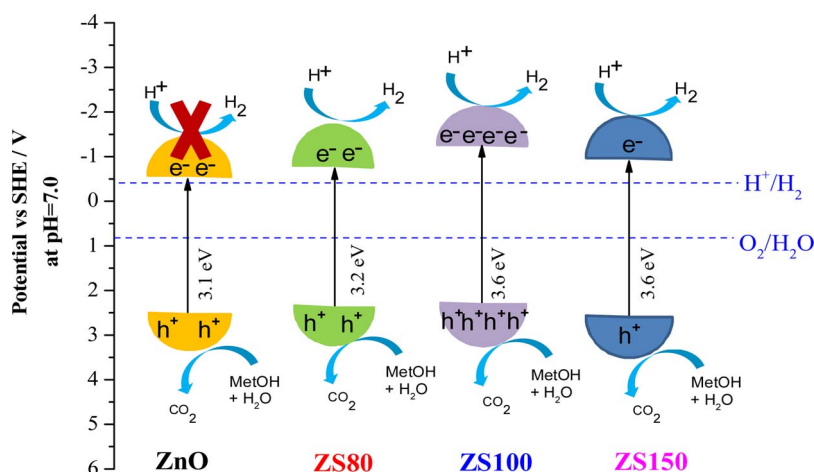
Fig. 10. Schematic representation of the position of the valence and conduction bands of the sulfided materials, as well as the reference material **ZnO**, in methanol-water solution (1:1 vol.).

energetic states are created at the interface, displacing the E_{fb} of the composite towards more negative values (see Table 2) favoring the reduction process from H^+ to H_2. The Fig. 10 shows the position of the valence and conduction band of **ZnO** and the sulfided materials. The conduction band position was obtained by approaching the E_{fb} (Table 2), and the valence band position was estimated by adding the band gap energy to E_{fb}, since, the E_g this is the minimum energy required to excite an electron from the valence band to the conduction band. On the other hand, although both ZnO and ZnS phases are present in the sulfided materials, only one valence and conduction band are shown for each one, because the ZnS-ZnO composite is a new material chemically linked through a heterojunction (see Fig. 6) with new physical and chemical properties different from the bare ZnO and ZnS photocatalysts, in this system, the band gap, the valence band and the conduction band can be tuned by modifications on the S/Zn composition. For both cases, water splitting and H_2 production using methanol as sacrificial agent, the reduction potential of the photogenerated electrons for the most active composite (**ZS100**) is more negative, so, there was a larger energy available to perform the H_2 production (see Table 2).

4. Conclusions

In this work a new method of synthesis is proposed to obtain the ZnS-ZnO composite active for H_2 production with and without sacrificial agent. The sulfided materials were synthesized by the solvothermal method at 80, 100, and 150 °C; the **ZS100** material was the most efficient, and presented an H_2 production of $247 \, \mu \text{mol h}^{-1} \text{g}^{-1}$ without sacrificial agent and using methanol as sacrificial agent, the hydrogen evolution increases up to five times, $1242 \, \mu \text{mol h}^{-1} \text{g}^{-1}$, using a UV Hg lamp of 254 nm. The improvement on the photocatalytic activity is attributed to the formation of the heterojunction between ZnS and ZnO, when the atomic ratio of S/Zn = 0.71. The heterojunction contributes to the accumulation of electrons at the conduction band, which are transferred to active sites for the reduction of H^+ to H_2. The photoelectrochemical characterization, proved that there is a shift on the reduction potential position towards more negative values for the **ZS80** and **ZS100** composites, this displacement favors the reduction processes on these photocatalysts, making the production of H_2 a more favorable process. The advantage of the solvothermal synthesis is that promotes a partial sulfidation of metal oxides with controllable composition at low temperatures. The ZnS-ZnO composite, promises to be an efficient photocatalyst for the H_2 production without using any sacrificial agent.

Appendix A. Supplementary data

Supplementary material related to this article can be found, in the online version, at doi:https://doi.org/10.1016/j.apcatb.2018.02.047.

References

[1] H. Ahmad, S.K. Kamarudin, L.J. Minggu, M. Kassim, Hydrogen from photo-catalytic water splitting process: a review, Renew. Sustain. Energy Rev. 43 (2015) 599–610.
[2] A.A. Ismail, D.W. Bahnemann, Photochemical splitting of water for hydrogen production by photocatalysis: a review, Sol. Energy Mater. Sol. Cells 128 (2014) 85–101.
[3] M. Reza Gholipour, C.-T. Dinh, F. Beland, T.-O. Do, Nanocomposite heterojunctions as sunlight-driven photocatalysts for hydrogen production from water splitting, Nanoscale 7 (2015) 8187–8208.
[4] Y. Tachibana, L. Vayssieres, J.R. Durrant, Artificial photosynthesis for solar water-splitting, Nat. Photon. 6 (2012) 511–518.
[5] H. Zhou, X. Li, T. Fan, F.E. Osterloh, J. Ding, E.M. Sabio, D. Zhang, Q. Guo, Artificial inorganic leafs for efficient photochemical hydrogen production inspired by natural photosynthesis, Adv. Mater. 22 (2010) 951–956.
[6] P. Fornasiero, K.C. Christoforidis, Photocatalytic hydrogen production: a rift into the future energy supply, ChemCatChem 9 (2017) 1523–1544.
[7] A.V. Puga, Photocatalytic production of hydrogen from biomass-derived feedstocks, Coord. Chem. Rev. 315 (2016) 1–66.
[8] E.A. Kozlova, V.N. Parmon, Heterogeneous semiconductor photocatalysts for hydrogen production from aqueous solutions of electron donors, Russ. Chem. Rev. 86 (2017) 870.
[9] S.J.A. Moniz, S.A. Shevlin, D.J. Martin, Z.-X. Guo, J. Tang, Visible-light driven heterojunction photocatalysts for water splitting–a critical review, Energy Environ. Sci. 8 (2015) 731–759.
[10] D. Xu, Y. Hai, X. Zhang, S. Zhang, R. He, Bi_2O_3 cocatalyst improving photocatalytic hydrogen evolution performance of TiO_2, Appl. Surf. Sci. 400 (2017) 530–536.
[11] D.P. Kumar, S. Hong, D.A. Reddy, T.K. Kim, Ultrathin MoS_2 layers anchored exfoliated reduced graphene oxide nanosheet hybrid as a highly efficient cocatalyst for CdS nanorods towards enhanced photocatalytic hydrogen production, Appl. Catal. B 212 (2017) 7–14.
[12] M. Gopannagari, D.P. Kumar, D.A. Reddy, S. Hong, M.I. Song, T.K. Kim, In situ preparation of few-layered WS_2 nanosheets and exfoliation into bilayers on CdS nanorods for ultrafast charge carrier migrations toward enhanced photocatalytic hydrogen production, J. Catal. 351 (2017) 153–160.
[13] Y. Piña-Pérez, F. Tzompantzi-Morales, R. Pérez-Hernández, R. Arroyo-Murillo, P. Acevedo-Peña, R. Gómez-Romero, Photocatalytic activity of Al_2O_3 improved by the addition of Ce^{3+}/Ce^{4+} synthesized by the sol-gel method. Photodegradation of phenolic compounds using UV light, Fuel 198 (2017) 11–21.
[14] A. Kudo, Y. Miseki, Heterogeneous photocatalyst materials for water splitting, Chem. Soc. Rev. 38 (2009) 253–278.
[15] O. Aguilar-Martínez, A. Hernández-Gordillo, R. Pérez-Hernández, P. Acevedo-Peña, A. Arrieta-Castañeda, R. Gómez, F. Tzompantzi, Efficient $ZnO_{1-x}S_x$ composites from

the $Zn_5(CO_3)_2(OH)_6$ precursor for the H_2 production by photocatalysis, Renew. Energy 113 (2017) 43–51.

[16] X. Gao, J. Wang, J. Yu, H. Xu, Novel ZnO-ZnS nanowire arrays with hetero-structures and enhanced photocatalytic properties, CrystEngComm 17 (2015) 6328–6337.

[17] E. Hong, J.H. Kim, Oxide content optimized ZnS-ZnO heterostructures via facile thermal treatment process for enhanced photocatalytic hydrogen production, Int. J. Hydrogen Energy 39 (2014) 9985–9993.

[18] J.S. Jang, C.J. Yu, S.H. Choi, S.M. Ji, E.S. Kim, J.S. Lee, Topotactic synthesis of mesoporous ZnS and ZnO nanoplates and their photocatalytic activity, J. Catal. 254 (2008) 144–155.

[19] A. Kushwaha, M. Aslam, ZnS shielded ZnO nanowire photoanodes for efficient water splitting, Electrochim. Acta 130 (2014) 222–231.

[20] Y. Liu, Y. Gu, X. Yan, Z. Kang, S. Lu, Y. Sun, Y. Zhang, Design of sandwich-struc-tured ZnO/ZnS/Au photoanode for enhanced efficiency of photoelectrochemical water splitting, Nano Res. 8 (2015) 2891–2900.

[21] H.X. Sang, X.T. Wang, C.C. Fan, F. Wang, Enhanced photocatalytic H_2 production from glycerol solution over ZnO/ZnS core/shell nanorods prepared by a low tem-perature route, Int. J. Hydrogen Energy 37 (2012) 1348–1355.

[22] Z. Wang, S.W. Cao, S.C.J. Loo, C. Xue, Nanoparticle heterojunctions in ZnS-ZnO hybrid nanowires for visible-light-driven photocatalytic hydrogen generation, CrystEngComm 15 (2013) 5688–5693.

[23] A. Wu, L. Jing, J. Wang, Y. Qu, Y. Xie, B. Jiang, C. Tian, H. Fu, ZnO-dotted porous ZnS cluster microspheres for high efficient, Pt-free photocatalytic hydrogen evo-lution, Sci. Rep. 5 (2015) 1–9.

[24] H. Zhao, Y. Dong, P. Jiang, X. Wu, R. Wu, Y. Chen, Facile preparation of a ZnS/ZnO nanocomposite for robust sunlight photocatalytic H_2 evolution from water, RSC Adv. 5 (2015) 6494–6500.

[25] W. Chen, H. Ruan, Y. Hu, D. Li, Z. Chen, J. Xian, J. Chen, X. Fu, Y. Shao, Y. Zheng, One-step preparation of hollow ZnO core/ZnS shell structures with enhanced photocatalytic properties, CrystEngComm 14 (2012) 6295–6305.

[26] L. Neveux, D. Chiche, J. Perez-Pellitero, L. Favergeon, A.-S. Gay, M. Pijolat, New insight into the ZnO sulfidation reaction: mechanism and kinetics modeling of the ZnS outward growth, Phys. Chem. Chem. Phys. 15 (2013) 1532–1545.

[27] D. Guerrero-Araque, P. Acevedo-Pena, D. Ramirez-Ortega, R. Gomez, Improving photocatalytic reduction of 4-nitrophenol over ZrO_2-TiO_2 by synergistic interaction between methanol and sulfite ions, New J. Chem. 41 (2017) 12655–12663.

[28] A. Coelho, TOPAS-Academic V4. 1, Coelho Software, Brisbane, Australia, 2007.

[29] L.E. Smart, E.A. Moore, Solid State Chemistry: an Introduction, CRC press, 2012.

[30] O. Aguilar, F. Tzompantzi, R. Pérez-Hernández, R. Gómez, A. Hernández-Gordillo, Novel preparation of ZnS from $Zn_5(CO_3)_2(OH)_6$ by the hydro or solvothermal method for H_2 production, Catal. Today 287 (2017) 91–98.

[31] S. Bagheri, K. Chandrappa, S.B.A. Hamid, Facile synthesis of nano-sized ZnO by direct precipitation method, Der Pharm. Chem. 5 (2013) 265–270.

[32] D. Japić, M. Bitenc, M. Marinšek, Z.C. Orel, The impact of nano-milling on porous ZnO prepared from layered zinc hydroxide nitrate and zinc hydroxide carbonate, Mater. Res. Bull. 60 (2014) 738–745.

[33] D. Liu, Y. Lv, M. Zhang, Y. Liu, Y. Zhu, R. Zong, Y. Zhu, Defect-related

photoluminescence and photocatalytic properties of porous ZnO nanosheets, J. Mater. Chem. A 2 (2014) 15377–15388.

[34] J. Liu, Z. Guo, F. Meng, T. Luo, M. Li, J. Liu, Novel porous single-crystalline ZnO nanosheets fabricated by annealing $ZnS(en)_{0.5}$ (en = ethylenediamine) precursor. Application in a gas sensor for indoor air contaminant detection, Nanotechnology 20 (2009) 125501.

[35] S. Kawar, B. Pawar, Nanocrystalline grain size in ZnS thin films deposited by che-mical bath technique, J. Mater. Sci.-Mater. Electron. 21 (2010) 906–909.

[36] C. Klingshirn, ZnO: material, physics and applications, ChemPhysChem 8 (2007) 782–803.

[37] W. Luo, S. Ismail-Beigi, M.L. Cohen, S.G. Louie, Quasiparticle band structure of ZnS and ZnSe, Phys. Rev. B 66 (2002) 195215.

[38] C. Wang, B. Klein, First-principles electronic structure of Si, Ge, GaP, GaAs, ZnS, and ZnSe. I. Self-consistent energy bands, charge densities, and effective masses, Phys. Rev. B 24 (1981) 3393.

[39] M. Thommes, K. Kaneko, A.V. Neimark, J.P. Olivier, F. Rodriguez-Reinoso, J. Rouquerol, K.S. Sing, Physisorption of gases, with special reference to the eva-luation of surface area and pore size distribution (IUPAC technical report), Pure Appl. Chem. 87 (2015) 1051–1069.

[40] K. Barick, S. Singh, M. Aslam, D. Bahadur, Porosity and photocatalytic studies of transition metal doped ZnO nanoclusters, Microporous Mesoporous Mater. 134 (2010) 195–202.

[41] W. Jia, B. Jia, F. Qu, X. Wu, Towards a highly efficient simulated sunlight driven photocatalyst: a case of heterostructured ZnO/ZnS hybrid structure, Dalton Trans. 42 (2013) 14178–14187.

[42] X. Li, X. Li, B. Zhu, J. Wang, H. Lan, X. Chen, Synthesis of porous ZnS, ZnO and ZnS/ZnO nanosheets and their photocatalytic properties, RSC Adv. 7 (2017) 30956–30962.

[43] X.-L. Yu, J.-G. Song, Y.-S. Fu, Y. Xie, X. Song, J. Sun, X.-W. Du, ZnS/ZnO hetero-nanostructure as photoanode to enhance the conversion efficiency of dye-sensitized solar cells, J. Phys. Chem. C 114 (2010) 2380–2384.

[44] G.R. Bamwenda, S. Tsubota, T. Nakamura, M. Haruta, Photoassisted hydrogen production from a water-ethanol solution: a comparison of activities of Au-TiO_2 and Pt-TiO_2, J. Photochem. Photobiol. A 89 (1995) 177–189.

[45] T. Lyubina, E. Kozlova, New photocatalysts based on cadmium and zinc sulfides for hydrogen evolution from aqueous Na_2S-Na_2SO_3 solutions under irradiation with visible light, Kinet. Catal. 53 (2012) 188–196.

[46] X. Zong, G. Lu, L. Wang, Nanocatalysts for water splitting, Nanocatal. Synth. Appl. (2013) 495–559.

[47] D. Guerrero-Araque, D. Ramírez-Ortega, P. Acevedo-Peña, F. Tzompantzi, H.A. Calderón, R. Gómez, Interfacial charge-transfer process across ZrO_2-TiO_2 heterojunction and its impact on photocatalytic activity, J. Photochem. Photobiol. A 335 (2017) 276–286.

[48] E.A. Kozlova, S.V. Cherepanova, D.V. Markovskaya, A.A. Saraev, E.Y. Gerasimov, V.N. Parmon, Novel photocatalysts Pt/$Cd_{1-x}Zn_xS$/ZnO/$Zn(OH)_2$: activation during hydrogen evolution from aqueous solutions of ethanol under visible light, Appl. Catal., B 183 (2016) 197–205.